Topology optimization for heat transfer enhancement in Latent Heat Thermal Energy Storage

Topology optimization for heat transfer enhancement in Latent Heat Thermal Energy Storage

Alberto Pizzolato[a,*], Ashesh Sharma[b], Kurt Maute[b], Adriano Sciacovelli[c], Vittorio Verda[a]

[a] *Department of Energy, Politecnico di Torino, Corso Duca degli Abruzzi 24, Turin, Italy*
[b] *Department of Aerospace Engineering Sciences, University of Colorado at Boulder, Boulder, CO, USA*
[c] *Birmingham Center for Energy Storage (BCES), School of Chemical Engineering, University of Birmingham, UK*

Abstract

Performance of a Latent Heat Thermal Energy Storage depends strongly on the spatial layout of high conductive material and phase change material. Previous design studies have explored a limited design space and have rarely taken advantage of any formal optimization approach. This paper presents a topology optimization framework of a Thermal Energy Storage system involving phase change. We solve the Stefan problem for solidification with a fixed grid finite element method based on the apparent heat capacity technique, while the topology optimization problem is formulated using a density-based method. This approach allows to identify design trends that have been rarely investigated in the past. Firstly, we explore the inherent trade-off between discharged energy and required time for complete discharge. We obtain very different designs and highly varying performances at selected Pareto points. Secondly, by comparing results obtained in two and three dimensions we observe that 3D designs allow superior performances by presenting features that are not apparent in 2D. Thirdly, we propose a formulation of the design problem that yields a nearly constant thermal power output during the entire discharge process. If the maximum discharge time is sufficiently large, the optimized design presents fins that are disconnected from the internal tube.

Keywords: Heat Transfer Enhancement, Phase Change Material, Thermal Energy Storage, Topology Optimization

*Corresponding author: alberto.pizzolato@polito.it

Nomenclature

$H^{(0)}$	Initial total enthalpy
N_s	Number of design variables
T	Temperature
T^h	Approximated temperature field
Z	Storage unit height
$\mathbf{J}$	Jacobian matrix
$\mathbf{R}$	Residual vector
$\tilde{s}$	Filtered design variable
c_p	Specific heat
f	Liquid fraction
f^*	Liquid fraction defined with dimensionless temperature
h	Specific enthalpy
k	Thermal conductivity
l	Characteristic length
p	Material interpolation exponent
q_v	Volumetric heat generation
r_1	Internal tube radius
r_2	External shell radius
r_f	Filter radius
s	Design variable
t	Time
v^h	Admissible test function
z	Objective function

Dimensionless groups

Fo	Fourier number
Ste	Stefan number

Greek symbols

α	Thermal diffusivity
β	Projection steepness parameter
$\boldsymbol{\lambda}$	Adjoint vector
η	Projection threshold
Γ	Boundary
Ω	Domain
ω	Filter weight
Φ	Desired volume fraction
Ψ	Desired fraction of initial energy
ρ	Density
ρ_s	Projected design variable
ξ	Logistic function constant

Superscripts

$*$	Dimensionless

Subscripts

d	Dirichlet
I	Initial
id	Ideal
m	Melting
max	Maximum
min	Minimum
N	Neumann

1. Introduction

Thermal Energy Storage (TES) plays a crucial role in modern energy systems. It allows reducing the temporal mismatch between energy supply and demand, resulting in a more rational use of resources. Among the available options, Latent Heat Thermal Energy Storage (LHTES) systems comprised of phase change materials (PCMs) show two of the most desirable properties for heat storage systems: *high energy density*, which allows the construction of compact designs well-suited for distributed applications [1], and *minimal operating temperature variation*, which yields a nearly constant efficiency of the heat transfer device during the entire charge/discharge process. These properties make PCM ideal also for other applications, e.g. space heating and cooling [2–4], solar energy technology [5], thermal management in Li-Ion batteries [6] and electronics cooling [7, 8]. For further information on thermal energy storage with phase change materials the reader is referred to state-of-the-art reviews such as those by Zalba et al. [9], Sharma et al. [10] and Kalnaes et al. [11].

Despite the aforementioned advantages, the use of LHTES is still hampered by its poor heat transfer properties. Most of the PCMs suffer from very low thermal conductivity, which limits the achievable heat transfer rate and reduces the spectrum of feasible applications [12]. To resolve this issue, the engineering community has followed different approaches, for instance addition of carbon additives [13], dispersion of high conductivity nanoparticles [14, 15], utilization of steel lessing rings [16] or high-porosity metal matrices [17], microencapsulation in partially melting/solidifying slurries [18], adoption of multi-tubes configurations [19–21], and increase of heat transfer surface area with highly conductive fins. The latter approach is the most widely adopted because of its simplicity, low construction cost, and ease of fabrication and maintenance [22].

One of the first numerical studies concerning heat transfer surfaces embedded in PCM was conducted by Smith et al [23], who used the finite difference method to solve the solidification problem adjacent to a cold fin and analyzed the effect of fin dimensions. Lacroix [24] developed a more accurate model based on the enthalpy formulation that also accounts for convective heat transfer from the Heat Transfer Fluid (HTF) and conducted a parametric analysis to investigate the effect of design and control variables such as the external envelope size and the HTF mass flow rate. The increasing availability of computational resources allowed researchers to progressively explore the influence of a greater

number of parameters. For instance, Ismail et al.[25] studied the influence of the number of fins, their length and thickness on the time of complete phase change. In [26] the authors proposed the utilization of Artificial Neural Network (ANN) trained with experimental data to quickly conduct heat transfer analysis for different heat transfer areas and HTF operative conditions. More recently, Tay et al.[27] compared heat transfer enhancement in solidification through radial fins and pins in multiple configurations. They found that the complete solidification time is roughly 25 % lower in the case of radial fins. Hosseini et al.[28] conducted a numerical and experimental investigation on longitudinally finned shell-and-tube LHTES, studying the relative effect of fin height and Stefan number. Their results showed that increasing the fin height leads to higher rate of heat absorption especially at the beginning of the charging process and for low Stefan numbers.

From the great amount of literature devoted to the analysis of finned surfaces for phase change materials it is hard to extract fundamental design guidelines. Most of the reviewed works are characterized by high physics complexity and low design freedom. The literature lacks a thorough and computationally affordable design optimization procedure for LHTES systems. A first study in this direction was conducted by Sciacovelli et al.[29] through a combination of a 2D transient finite volume physical model and response surface optimization method[30]. It was found that the discharge efficiency can be increased by 24 % if optimal fins with two bifurcations are chosen. In a more recent development, a heuristic pseudo-optimization procedure based on the analysis of the entropy generation maps was used [31]. With this approach they were able to obtain an optimized fin tilt angle along the longitudinal direction which allows to halve the solidification time. Despite the importance of these studies for the development of optimization procedures for LHTES systems, they are still restricted to a low-dimensional design space [29]. This paper aims towards filling this gap in the literature.

Topology optimization allows for dramatic design changes during the optimization process and does not require a close to optimal design to start with. The method originated in the structural community with the pioneering work of Bendsoe [32], Zhou and Rozvany [33] who suggested the SIMP (Solid Isotropic Material with Penalization) or power-law approach. They introduced a fictitious porous material with normalized density ρ to define a continuous transition between two or more phases. This normalized density interpolates the material properties and is used as an optimization variable. The interpolation is formulated to penalize intermediate densities and converge to designs with well-distinct phases. Besides this "density" approach, topology optimization developed in alternative directions, e.g. level set [34, 35], evolutionary approaches [36, 37] and several others [38]. The method gained maturity in the structural community and quickly extended to many other fields such as fluid-dynamics [39–41], acoustics [42], bending waves propagation [43], aero-elasticity [44], electromagnetics [45] and meta-materials design [46]. Early interests in the field of heat transfer come from the fact that the problem of optimal design of heat dissipators undergoing steady-state conduction is a trivial extension of the

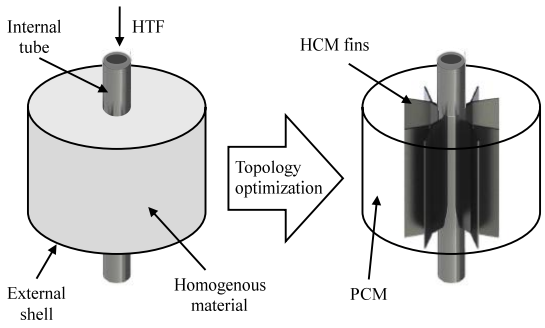

Figure 1. Representative visualization of optimization of finning material distribution in LHTES. The Heat Transfer Fluid flows in the tube while the PCM occupies the external envelope

typical compliance minimization problem for structural design [47]. Later on, more complicated heat transfer mechanisms were studied e.g. forced convection [48, 49], natural convection [50, 51] and radiation [52].

Although steady-state heat conduction problems has been tackled extensively, few studies [53, 54] have considered transient effects. To date, only one work [55] has exploited topology optimization to enhance heat transfer during phase change. The authors presented novel and nonintuitive designs of PCM-based fin heat sinks. The objective of the optimization problem was to minimize the difference between the final and initial temperatures over a selected portion of the domain. Their approach requires defining an a-priori fixed final time for the calculation of the final temperature. The definition of this final time is not trivial since the characteristic melting/solidification time is inherently design-dependent. Furthermore their work suffers from poor resolution due to the limited computational performance achievable at the time.

In this paper we present the first study of topology optimization to the design of highly conductive fins in shell-and-tube LHTES. We propose a novel optimization problem formulation that does not require an a-priori definition of the final time. We focus on solidification because the average heat transfer rate is significantly lower than in melting [29]. The inherent flexibility of this approach allows us to explore the dependency of the optimized design on important parameters such as the choice of the desired discharge time, the choice of the desired discharged energy and the steadiness of the thermal power output. A schematic of the density-based topology optimization procedure for the problems considered is given in Figure 1. A vertical tube filled with a cold HTF stream is surrounded by both a low conductive PCM and a Highly Conductive Material (HCM). The spatial distribution of the latter in the external shell is initialized as homogeneous. As the optimization process evolves, HCM is locally added and removed until the optimized finned geometry is obtained.

The remainder of this paper is organized as follows: Section 2 presents the governing equations along with the temporal and spatial discretization schemes.

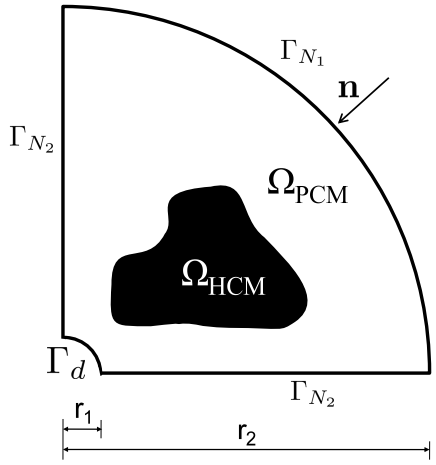

Figure 2. Representative configuration of the optimization problem considered

Section 3 presents the numerical optimization problem solved including the sensitivity analysis and other details concerning the adopted optimization approach. Section 4 presents numerical examples to validate and analyze the proposed approach. Finally, a summary and concluding remarks are presented in Section 5.

2. Physical model

In this section we provide a description of the physical problem solved including the governing equations, followed by the spatial and temporal discretization approaches adopted.

2.1. Governing equations

In this paper, we optimize the discharge process of a domain consisting of two materials, the HCM and the PCM, in both 2D and 3D. Figure 2 shows a representative configuration of the problem considered: the design domain Ω_D consists of a quarter of the TES cross-section (Figure 1), which is subdivided into two non-overlapping sub-domains Ω_{HCM} and Ω_{PCM} such that $\Omega_D = \Omega_{HCM} \cup \Omega_{PCM}$. The temperature T_d is prescribed at the internal boundary Γ_d to represent contact with the tube containing a cold HTF while a homogeneous Neumann boundary condition is prescribed on Γ_{N_1} to describe an adiabatic boundary (external envelope) and on Γ_{N_2} to account for symmetry. The solidification process is dominated by heat conduction. Natural convection can be neglected except for the very initial part of the process [56]. Hence we consider the solidification of PCM as modeled by pure thermal diffusion using

the enthalpy form of the energy equation:

$$\frac{\partial(\rho(\mathbf{x})h(\mathbf{x}))}{\partial t} = \frac{\partial}{\partial x_i}\left(k_{ij}(\mathbf{x})\frac{\partial T}{\partial x_j}\right) + q_v \qquad in \quad \Omega_{HCM} \cup \Omega_{PCM} \tag{1}$$

where h is the specific enthalpy, ρ is the density, k_{ij} is the (i, j) component of the conductivity tensor and q_v is the volumetric heat generation. The material properties correspond to HCM when $\mathbf{x} \in \Omega_{HCM}$ and to PCM when $\mathbf{x} \in \Omega_{PCM}$. The time-independent Dirichlet and Neumann boundary conditions are given by:

$$T = T_d \qquad on \quad \Gamma_d, \quad \forall t \tag{2}$$

$$\left(-k_{ij}\frac{\partial T}{\partial x_j}\right) \cdot \mathbf{n} = \mathbf{q}_N \qquad on \quad \Gamma_{N_1} \cup \Gamma_{N_2}, \quad \forall t \tag{3}$$

where $\mathbf{q}_N$ is the applied heat flux and $\mathbf{n}$ is the inward pointing normal on Ω_D. The space-independent initial conditions are:

$$T = T_I \qquad in \quad \Omega_{HCM} \cup \Omega_{PCM}, \quad \text{at } t = 0 \tag{4}$$

The term on the left-hand side of Eq. 1 accounts for the energy accumulation in the form of both sensible and latent heat. The enthalpy of a solid can be written as:

$$h(T) = \int_{T_{ref}}^{T} c_p(T)dT + f(T)L \tag{5}$$

where T_{ref} is a reference temperature, c_p is the specific heat and f is a temperature-dependent phase function that keeps track of the amount of material that is in the liquid phase. In the present work we use the logistic distribution to represent f as:

$$f(T) = \frac{1}{1 + \exp(-\xi(T - T_m))} \tag{6}$$

where T_m is the mean melting temperature and $\xi = 30$ is a constant that controls the steepness of the logistic curve and is dependent on the width of the mushy zone.

2.2. Dimensionless form

We consider temperature-independent thermo-physical properties, isotropic thermal conductivity and ignore internal heat generation. With these assumptions, by substituting Eq. (5) into Eq. (1) and applying the chain rule of differentiation to the latent heat portion of enthalpy we obtain:

$$\left(\rho c_p + \rho L\frac{\partial f}{\partial T}\right)\frac{\partial T}{\partial t} = \frac{\partial}{\partial x_i}\left(k\delta_{ij}\frac{\partial T}{\partial x_j}\right) \tag{7}$$

where δ_{ij} is the Kronecker delta. Eq. (7) is cast in dimensionless settings using the following dimensionless variables:

- Dimensionless time (Fourier number):

$$t^* = \frac{\alpha_{PCM} t}{l^2} = Fo \tag{8}$$

- Dimensionless coordinate:

$$x_i^* = \frac{x_i}{l} \tag{9}$$

- Dimensionless temperature:

$$T^* = \frac{T - T_{min}}{T_{max} - T_{min}} \tag{10}$$

- Dimensionless latent heat (phase transition number):

$$L^* = \frac{L}{c_{pPCM}(T_{max} - T_{min})} = \frac{1}{Ste} \tag{11}$$

where l is the characteristic length, α_{PCM} is the thermal diffusivity of the PCM, Fo is the Fourier number, Ste is the Stefan number, T_{max} and T_{min} are the maximum and minimum temperature of the entire discharging process. Substituting Eqs. (8) through (11) into Eq. (7) we obtain:

$$\left(C + \gamma L^* \frac{\partial f^*}{\partial T^*}\right) \frac{\partial T^*}{\partial t^*} = \frac{\partial}{\partial x_i^*}\left(K_{ij} \frac{\partial T^*}{\partial x_j^*}\right) \tag{12}$$

where:

$$C = \begin{cases} \frac{(\rho c_p)_{HCM}}{(\rho c_p)_{PCM}} & in \quad \Omega_{HCM} \\ 1 & in \quad \Omega_{PCM} \end{cases} \tag{13}$$

$$K_{ij} = \begin{cases} \frac{k_{HCM}}{k_{PCM}} \delta_{ij} & in \quad \Omega_{HCM} \\ \delta_{ij} & in \quad \Omega_{PCM} \end{cases} \tag{14}$$

$$\gamma = \begin{cases} 0 & in \quad \Omega_{HCM} \\ 1 & in \quad \Omega_{PCM} \end{cases} \tag{15}$$

and $f^* = f(T^*)$.

2.3. Spatial and temporal discretization

The residual of the weak form of the dimensionless nonlinear diffusion equation (Eq. (12)), R, is written as:

$$R = \int_{\Omega_D} v^h \left(C + \gamma L^* \frac{\partial f^*}{\partial T^*}\right) \frac{\partial T^h}{\partial t^*} dV - \int_{\Omega_D} \frac{\partial v^h}{\partial x_i^*} K_{ij} \frac{\partial T^h}{\partial x_i^*} dV - \int_{\Gamma_N} v^h q_n dA = 0 \tag{16}$$

where v^h denotes an admissible test function, T^h is the approximated temperature field and Γ_N is a generic Neumann boundary. We adopt the standard

Galerkin approach in defining the solution space $\mathcal{U}$ and the weighting space $\mathcal{V}$ such that:

$$\begin{aligned} \mathcal{U} &= \{T^h \in \mathcal{H}^1(\Omega_D);\ T^h = T_d^* \ \text{ on } \Gamma_d\}, \\ \mathcal{V} &= \{v^h \in \mathcal{H}^1(\Omega_D);\ v^h = 0 \ \text{ on } \Gamma_d\} \end{aligned} \tag{17}$$

where $\mathcal{U}$ and $\mathcal{V}$ are Hilbert spaces consisting of scalar functions with square integrable first derivatives. Equation (16) is then discretized in space to yield the semi-discrete form:

$$\mathbf{R}\left(\mathbf{T}^*, \dot{\mathbf{T}}^*\right) = 0 \tag{18}$$

where the vector $\mathbf{T}^*$ represents the discrete dimensionless temperature field and $\dot{\mathbf{T}}^*$ is its time-derivative. Eq. (18) is discretized in time with the backward Euler scheme. The time-derivative of the discrete dimensionless temperature field is written as:

$$\dot{\mathbf{T}}^{*(n)} = \left(\frac{\partial \mathbf{T}^*}{\partial t^*}\right)^{(n)} = \frac{\mathbf{T}^{*(n)} - \mathbf{T}^{*(n-1)}}{\Delta t^*}, \qquad n = 1, ..., N_t \tag{19}$$

where n is the time step index, N_t total number of time steps and Δt^* the time-step size. At time step $n = 0$ the discrete residual equations reduce to satisfy the initial conditions:

$$\mathbf{R}^{(0)} = \mathbf{T}^{*(0)} - \mathbf{T}^* \tag{20}$$

For every subsequent time-step when $n > 0$, we solve the nonlinear problem $\mathbf{R}^{(n)} = 0$ through Newton's method. The Jacobian $\mathbf{J}^{(n)}$ is obtained considering a static and a dynamic contribution:

$$\mathbf{J}^{(n)} = \left.\frac{\partial \mathbf{R}}{\partial \mathbf{T}^{*(n)}}\right|_{T^{(n)}} + \left.\frac{\partial \mathbf{R}}{\partial \dot{\mathbf{T}}^{*(n)}}\right|_{T^{(n)}} \frac{1}{\Delta t^*} \tag{21}$$

where the second term has been obtained considering the integration scheme adopted (Eq. (19)).

3. Optimization problem

This section discusses the optimization problem formulation along with the material interpolation and the corresponding sensitivity analysis. In addition we summarize the regularization approaches adopted.

3.1. Objective and constraints

The topology optimization problem for heat transfer enhancement in TES tanks can be written in three alternative forms that consider three different design requirements:

(i) *What is the optimal topology of HCM that allows discharging the maximum amount of energy from a given amount of PCM in a given time period?* The Energy Minimization approach aims at minimizing the residual energy (or enthalpy) $H(t_f^*)$ in the tank at an a-priori specified discharge time t_f^*. The optimization problem is formulated as:

$$\begin{aligned} \underset{\mathbf{s}}{\text{minimize}} \quad & z(\mathbf{T}^*(\mathbf{s}),\mathbf{s}) = \int_{\Omega_D} h^* \; dV \quad at \quad t^* = t_f^* \\ \text{subject to} \quad & \mathbf{R}\big(\mathbf{T}^*(\mathbf{s}),\mathbf{s}\big) = 0 \\ & \int_{\Omega_D} \rho_s(s) \; dV - \Phi \int_{\Omega_D} dV \leq 0 \\ & \mathbf{s} \in \mathbf{S} = \big\{\mathbb{R}^{N_s} \mid s_{min} < s_i < s_{max}, i = 1, ..., N_s\big\} \end{aligned} \tag{22}$$

where $h^* = T^* + f^* L^*$ is the specific dimensionless enthalpy, ρ_s is the normalized density of HCM, $\mathbf{s}$ is the vector of design variables, Φ the maximum volume fraction of HCM and N_s the number of design variables with upper and lower bounds denoted by s_{max} and s_{min} respectively. The design variable field $\mathbf{s}$ is discretized at the node level. The normalized HCM density ρ_s is obtained from a regularization of the $\mathbf{s}$ field as detailed in a later section. The inequality constraint, i.e. the volume constraint, aims at preventing the trivial solution of having the entire design domain filled with HCM. It should be noted that for isobaric-isochoric processes with no kinetic energy and gravitational forces involved we have $dh = de$, i.e. specific enthalpy changes correspond to specific internal energy changes.

(ii) *What is the optimal topology of HCM that allows discharging a given amount of energy from a given amount of PCM in the least time?* The Time Minimization approach aims at minimizing the time t_f^* needed to reach a specified residual energy fraction Ψ. The optimization problem is formulated as:

$$\begin{aligned} \underset{\mathbf{s}}{\text{minimize}} \quad & z(\mathbf{T}^*(\mathbf{s}),\mathbf{s}) = t_f^* \\ \text{subject to} \quad & \int_{\Omega_D} h^* dV - \Psi H^{(0)} = 0 \quad at \quad t^* = t_f^* \\ & \mathbf{R}\big(\mathbf{T}^*(\mathbf{s}),\mathbf{s}\big) = 0 \\ & \int_{\Omega_D} \rho_s(s) \; dV - \Phi \int_{\Omega_D} dV \leq 0 \\ & \mathbf{s} \in \mathbf{S} = \big\{\mathbb{R}^{N_s} \mid s_{min} < s_i < s_{max}, i = 1, ..., N_s\big\} \end{aligned} \tag{23}$$

where $H^{(0)}$ is the initial total dimensionless enthalpy in the tank defined as:

$$H^{(0)} = \int_{\Omega_D} h^* \; dV \qquad \text{at } t^* = 0 \tag{24}$$

Problem (23) can be solved with marginal algorithmic modifications with respect to Problem (22). It is easy to demonstrate that the design sensitivities of the two approaches only differ by a positive multiplication factor. Linearizing the enthalpy history around the final time t_f^*, we have

$$H(t^*) = H(t_f^*) + \left.\frac{dH}{dt^*}\right|_{t^*=t_f^*} \left(t^* - t_f^*\right) + O\left((t^* - t_f^*)^2\right) \tag{25}$$

Neglecting higher order terms we solve (25) for t_f^* and differentiate to obtain:

$$\frac{dt_f^*}{d\mathbf{s}} = \left(- \left.\frac{dH}{dt^*}\right|_{t^*=t_f^*} \right)^{-1} \frac{dH(t^*)}{d\mathbf{s}} \tag{26}$$

Note that Eq. (26) is obtained considering that $dH(t_f^*)/ds = 0$ because $H(t_f^*)$ is a constant in the Time Minimization procedure. Since we consider a discharge process the evolution of the enthalpy is a monotonically decreasing process thus making the denominator positive.
Figure 3(a) shows an intuitive representation of the above-mentioned concepts on two consecutive discharge histories along the optimization routine. Here $dH(t_f^*)$ represents a final energy gain in the Energy Minimization procedure while dt_f^* represents a final time gain in the Time Minimization procedure.

(iii) *What is the optimal topology of HCM fins that maximizes the steadiness of the TES discharge?* The Steadiness Maximization approach aims at minimizing the deviation of a real discharge curve $H(t^*)$ from an ideal one $H_{id}(t^*)$. In this case, the problem is formulated as:

$$\begin{aligned}
\underset{\mathbf{s}}{\text{minimize}} \quad & z(\mathbf{T}^*(\mathbf{s}), \mathbf{s}) = \int_0^{t_f^*} \left(H(t^*) - H_{id}(t^*) \right)^2 dt^* \\
\text{subject to} \quad & \mathbf{R}\big(\mathbf{T}^*(\mathbf{s}), \mathbf{s}\big) = 0 \\
& \int_{\Omega_D} \rho_s(s)\, dV - \Phi \int_{\Omega_D} dV \leq 0 \\
& t_f^* - t_{f_{id}}^* \leq 0 \\
& \mathbf{s} \in \mathbf{S} = \left\{ \mathbb{R}^{N_s} \mid s_{min} < s_i < s_{max}, i = 1, ..., N_s \right\}
\end{aligned} \tag{27}$$

where $t_{f_{id}}^*$ is the ideal discharge time. The ideal discharge curve $H_{id}(t^*)$ is defined as:

$$H_{id}(t^*) = \begin{cases} H^{(0)} - \frac{H^{(0)}(1-\Psi)}{t_{f_{id}}^*} t^* & \text{if } t^* \leq t_{f_{id}}^* \\ H^{(0)}\Psi & \text{if } t^* > t_{f_{id}}^* \end{cases} \tag{28}$$

The choice of a linear ideal enthalpy history $H_{id}(t^*)$ implies that the ideal thermal power output, i.e. dH_{id}/dt^*, is constant during the entire discharge. The second inequality constraint imposes a maximum limit on

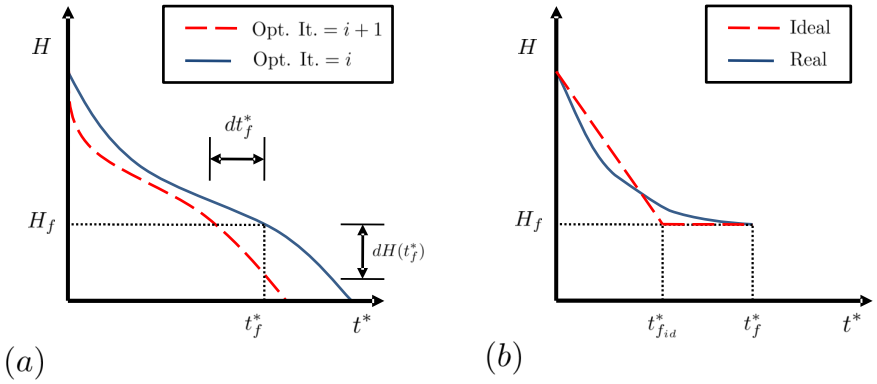

Figure 3. (a): Energy Minimization vs Time Minimization approach. (b): Steadiness Maximization approach

the discharge time and has the aim of providing control over this important design criterion to avoid undesirably lengthy discharge processes. Please note that the second case of (28), i.e. when $t^* > t^*_{f_{id}}$, is required for the correct objective function calculation in the non-feasible region, as shown in Fig. 3.(b).

3.2. Material interpolation

Density-based topology optimization requires an interpolation of the material properties such that the design process converges to binary designs. This is achieved by making intermediate values of the fictitious density ρ_s somewhat unattractive to the optimization routine via a penalty method.
In the present paper we use the conventional SIMP interpolation strategy to interpolate the conductivity term K :

$$K(s) = 1 + \left(\frac{k_{HCM}}{k_{PCM}} - 1\right)\rho_s^p \tag{29}$$

where the exponent p of the power-law interpolation has been set to 2. The nonlinearity of Eq. (29) combined with the linear volume constraint causes the penalization effect. We use a simple linear interpolation for the capacitance term C and the latent heat term L:

$$C(s) = 1 + \left(\frac{(\rho c_p)_{HCM}}{(\rho c_p)_{PCM}} - 1\right)\rho_s \tag{30}$$

$$L^*(s) = L^*_{PCM}\left(1 - \rho_s\right) \tag{31}$$

With this set-up good convergence to binary designs was observed in preliminary numerical tests performed.

3.3. Adjoint sensitivity analysis

The derivatives of the objective and constraints with respect to the design variables are needed for a gradient-based optimization method. Topology optimization is characterized by a high number of design variables and few constraints. Hence, the adjoint method is particularly convenient as it requires solving one additional linear problem per objective and constraint [57].

The discrete sensitivity field for the objective using the adjoint approach is calculated as:

$$\frac{dz}{d\mathbf{s}} = \frac{\partial z}{\partial \mathbf{s}} + \sum_{n=0}^{N_t} \boldsymbol{\lambda}^{(n)^T} \frac{\partial \mathbf{R}^{(n)}}{\partial \mathbf{s}} \tag{32}$$

where $\boldsymbol{\lambda}^{(n)}$ is the discrete adjoint field at time n, which is calculated by integrating the adjoint equation backward in time:

$$\left(\mathbf{J}^{(n)}\right)^T \boldsymbol{\lambda}^{(n)} = -\left(\frac{\partial z}{\partial \mathbf{T}^*}\right)^{(n)} + \frac{1}{\Delta t^{*(n+1)}} \left(\frac{\partial \mathbf{R}^{(n+1)}}{\partial \dot{\mathbf{T}}^{*(n+1)}}\bigg|_{T^{(n+1)}}\right)^T \boldsymbol{\lambda}^{(n+1)} \tag{33}$$

for $n = N_t, ..., 0$ and $\boldsymbol{\lambda}^{(N_t+1)} = \mathbf{0}$. As discussed in Section 3.1, the sensitivities for the Time Minimization problem are calculated by post-multiplying the sensitivities obtained for the Energy Minimization problem using (26). Hence, in Equation (33), $z = \int\limits_{\Omega_D} h^*(t_f^*)\, dV$ for both the Energy Minimization and the Time Minimization procedures. The adjoint method needs the forward solution for the computation of the adjoint states. For this reason, the forward solutions are stored for every time-step of the analysis. The adjoint solutions are calculated using the same time-steps adopted for the forward analysis. In this work the partial derivatives appearing in Eq. (32) are calculated through a central finite difference scheme. The partial derivatives of Eq. (33) are obtained by analytical differentiation of the discrete problem. A similar procedure is followed for the computation of constraint sensitivities.

3.4. Regularization

Filtering is a popular regularization approach in topology optimization that ensures both mesh-independence and checkerboard-free results [58]. We use a normalized linear density filter like the one originally proposed by [59]. The filtered nodal density field at node i is calculated as:

$$\widetilde{s}_i = \left(\sum_{j=1}^{N_s} \omega_{ij}\right)^{-1} \sum_{j=1}^{N_s} \omega_{ij} s_j \tag{34}$$

where N_s is the number of nodes in the complete mesh and ω_{ij} is the filter weight calculated as:

$$\omega_{ij} = max\Big(0, r_f - |\mathbf{x}_i - \mathbf{x}_j|\Big) \tag{35}$$

where r_f is the prescribed filter radius. The filter introduces some additional fuzziness in the design, i.e. it *smooths* the normalized density gradients and smears the two-material interface. Several projection schemes have been proposed to solve this issue and obtain crisp boundaries. Here we use the one proposed by Wang et al.[60]:

$$\rho_{s_i} = \frac{\tanh\Big(\beta\eta\Big) + \tanh\Big(\beta(\widetilde{s}_i - \eta)\Big)}{\tanh\Big(\beta\eta\Big) + \tanh\Big(\beta(1-\eta)\Big)} \tag{36}$$

where $\eta = 0.5$ represents the projection threshold while $\beta = 1$ is a parameter that controls the steepness of the projection. Note that this choice of parameters results in a mild projection that does not provide any feature size control. The projected density field $\boldsymbol{\rho}_s$ represents now the physical design variable set which is used in (30), (31) and (29) to interpolate the thermo-physical problems. We account for the filtering scheme in the sensitivity analysis by applying the chain rule as following:

$$\frac{\partial z}{\partial s_i} = \sum_{j=1}^{N_s}\sum_{k=1}^{N_s} \frac{\partial z}{\partial \rho_{s_k}} \frac{\partial \rho_{s_k}}{\partial \widetilde{s}_j} \frac{\partial \widetilde{s}_j}{\partial s_i} \tag{37}$$

4. Results and discussion

This section presents and discusses the results obtained for three different numerical studies. The first study focuses on the energy-time trade-off that arises during the optimization of LHTES systems. The second study is a 3D extension of the first example. The third study investigates the possibility of tuning the discharge process to obtain a constant thermal power output. The set of nonlinear equations arising from the spatial and temporal discretization are solved via the under-relaxed Newton method. The optimal value of the under-relaxation parameter depends on the degree of non-linearity of the problem, hence on the L/c_p ratio. Numerical experiments have shown that 0.95 is a good trade-off between reliable convergence and computational cost. Convergence is considered satisfactory when the relative residuals L_2 norm drops below 1e-7.

At each Newton iteration, the system of linearized equations is solved via the Unsymmetric-pattern MultiFrontal method (UMFPACK [61]) for the 2D problems described in this paper. For the 3D problems, we use the more efficient Generalized Minimal RESidual (GMRES) iterative method [62], with an Incomplete LU factorization and dual Threshold (ILUT) preconditioner [63]. Time integration is performed through an adaptive scheme. If Newton's method does not convergence within the first 15 iterations, the time step is iteratively halved until convergence is reached. The original time-step is restored after 5 successful time iterations at the reduced time-step. The optimization problems are solved using the Globally Convergent Method of Moving Asymptotes (GCMMA) of Svanberg et al. [64]. The general idea behind the GCMMA is to solve a series of convex and separable subproblems obtained from the original

Table 1. GCMMA parameters utilized

Parameter	Value
Step-size	0.03
Minimum asymptote adaptivity	0.5
Initial asymptote adaptivity	0.7
Maximum adaptivity	1.43
Constraint penalty	1000

Table 2. Thermo-physical properties of materials in dimensionless settings

Description	Parameter
Conductivity ratio	$\frac{k_{HCM}}{k_{PCM}} = 600$
Capacitance ratio	$\frac{(\rho c_p)_{HCM}}{(\rho c_p)_{PCM}} = 1.6$
Dimensionless Latent heat	$L^* = 20$
Dimensionless melting temperature	$T_m^* = 0.5$

problem. To ensure feasibility, some elastic (design) variables are introduced in the problem. In the present framework, the GCMMA subproblems are solved with a primal-dual method. The relevant GCMMA parameters are provided in Table 1. Convergence is considered satisfactory when the relative change in the objective drops below 1e-6 and all constraints are satisfied.

For the 2D problems, the computational domain consists of a quarter of the TES cross section (Fig. 2) with $r_1 = 0.1$ and $r_2 = 1$. We use a computational mesh with 11970 quadrilateral bilinear elements with angular size $\Delta\theta = 1^\circ$ and radial size $\Delta r = r\Delta\theta$. The 3D mesh is a lateral extension of the 2D mesh with $\Delta z = 0.071$ in the thickness direction and has a total of 507000 hexahedral trilinear elements. The height Z of the quarter hollow cylinder is set to 3. By considering a quarter of the cross section, we restrict the design domain and enforce θ-periodic optimized designs with period $\Theta = 90^\circ$. However, in analogous optimization runs performed with $\Theta = \{120^\circ;\ 180^\circ;\ 360^\circ\}$, the optimized objective revealed to be only insignificantly sensitive to the Θ choice. In the cases considered, the optimized objective increase with respect to the $\Theta = 90^\circ$ case ranged from a minimum of -0.1 % to a maximum of 1.2 %.

The accuracy of the presented framework is verified using a benchmark problem against the results obtained with the finite element commercial package COMSOL Multiphysics [65]. We simulate the discharge of a storage unit with the geometry shown in Figure 4(a). We use the same HCM and PCM used in a previous design optimization study of a medium-scale latent energy storage unit for district heating applications [29]. The relevant thermo-physical properties rewritten in non-dimensional form are presented in Table 2 while all the relevant analysis parameters are summarized in Table 3. Figure 4(b) shows the temperature profile along the red line highlighted in Figure 4(a) at different time instants, i.e. $t^* = [0.01,\ 0.05,\ 0.09,\ 0.13,\ 0.17]$. We observe that the thermal response predicted by the current framework agrees well with the

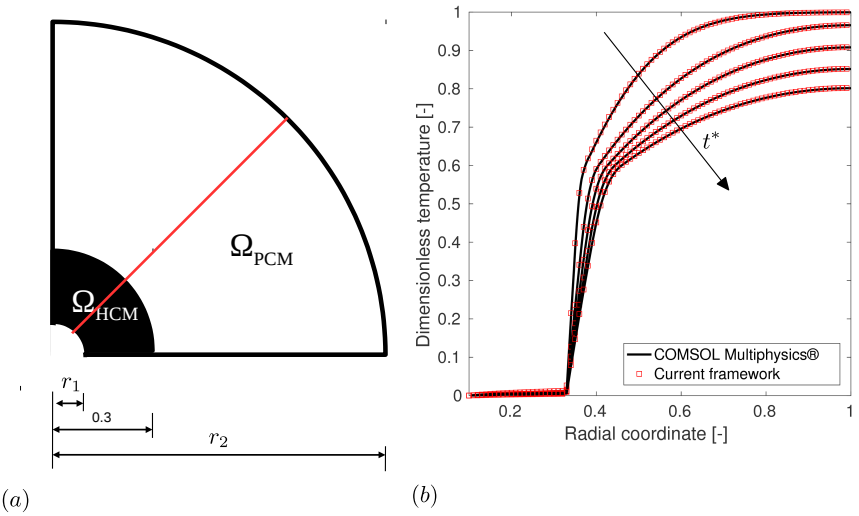

Figure 4. Verification test against COMSOL Multiphysics. (a): Schematics of the geometry considered. (b): Comparison of the temperature profiles at $t^* = [0.01,\ 0.05,\ 0.09,\ 0.13,\ 0.17]$

Table 3. Relevant analysis parameters

Description	Parameter
Boundary heat flux	$\mathbf{q}_n = \mathbf{0}$
Imposed temperature	$T_d = 0$
Initial temperature	$T_I = 1$

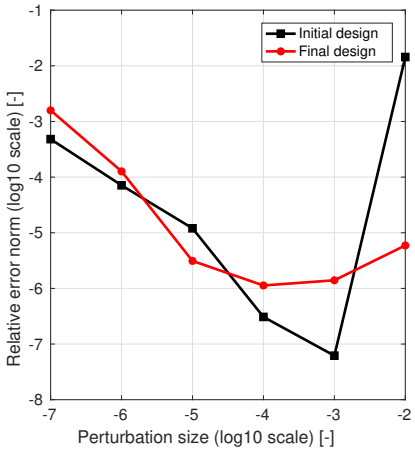

Figure 5. Comparison of design sensitivities computed by the adjoint method and by finite differencing

results obtained with COMSOL. The relative error L_2 norm is calculated to be $4.01 \cdot 10^{-4}$ with a standard deviation of $1.66 \cdot 10^{-4}$.

To verify the accuracy of the adjoint sensitivities, we performed (central) finite difference checks on 100 design variables in both the initial design (i.e. $s = 0.5$) and the optimized design for $\Psi = 5$ %, which will be described in Section 4.1. Figure 5 reports the L_2 norm of the relative error for different perturbation sizes used to calculate the finite difference sensitivities. The relative error is computed with respect to the value of the finite difference sensitivity. The minimum error is achieved for perturbation sizes of $\Delta s = 10^{-3}$ and $\Delta s = 10^{-4}$ for the initial and final design. Overall, we observe good agreement between analytical and finite difference sensitivities. This suggests the correctness of our analytical derivations and implementation.

4.1. Energy vs time trade-off

In this section we explore the inherent trade-off between the discharge time t_f^* and the target energy fraction Ψ. The thermo-physical properties and the analysis parameters are the same introduced for the verification study presented in the previous section (see Table 2 and 3). The maximum allowable volume fraction of HCM Φ is set to 10 %.

We solve the optimization problem using both the Time Minimization and Energy Minimization approach. To obtain the characteristic performance curves, we systematically relax the energy and time constraint for the first and second case respectively. First, we run the Time Minimization problem (23) setting the target energy fraction Ψ as 2.5 %, 5%, 10 %, 25 %, 50 % and 80 %. The final objective value, i.e. the optimized time required for the complete discharge, is then set as a constraint for the subsequent Energy Minimization procedure (22).

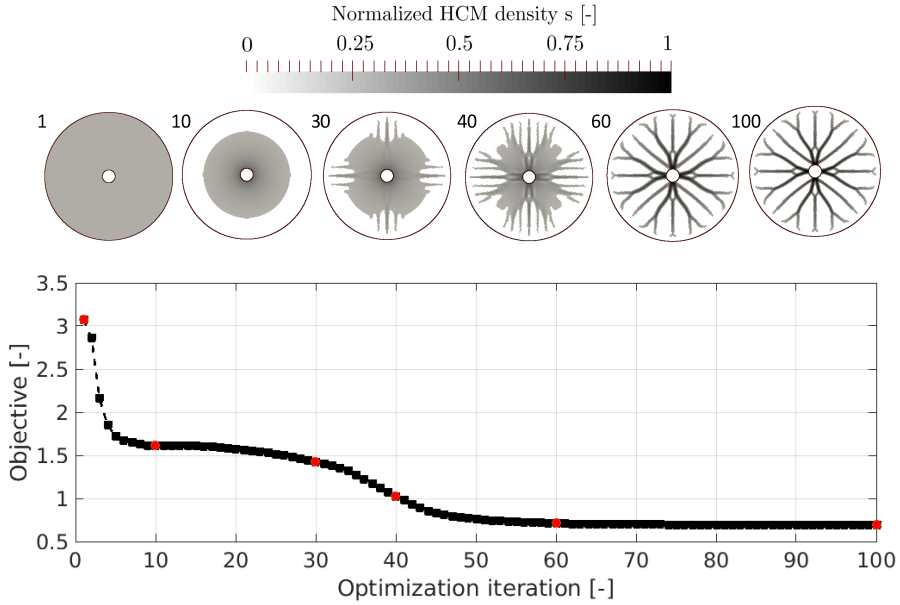

Figure 6. Objective history during the design optimization at $\Psi = 5\%$. The design evolution is shown at selected design iterations. The design snapshots are obtained exploiting the symmetry condition

The objective history during the Time Minimization optimization process for the case in which the target energy fraction Ψ is equal to 5 %, along with snapshots of the design at selected iterations is depicted in Figure 6. All designs presented in this paper correspond to density contour plots where only regions with $s \geq 0.1$ are shown. Also note that the same colorbar shown in Figure 6 is used for all the results presented in the following sections. The initial design (iteration 1) corresponds to a homogeneous material distribution $s = 0.1$ on the design domain Ω_D. The HCM quickly (i.e. in 5/6 design iterations) concentrates in a region close to the internal tube. Then the convergence rate slows down until some conductive branches break the problem symmetry (iteration 30), which is when we observe the second quick objective drop.

The designs obtained for the remaining cases are shown in Figure 7. As the target energy fraction Ψ increases, the characteristic length of fins decreases to occupy a smaller region close to the internal tube leaving a hot external shell. A closer examination of the designs at 80 %, 50 % and 25 % of initial energy reveals that the maximum length branch scales as $l_{max} \sim \sqrt{1-\Psi}$. Once the fins achieve the length corresponding to the radius of the external envelope, energy extraction is increased by accumulating HCM towards the external envelope: in the optimized designs for $\Psi = 10$ % and $\Psi = 2.5\%$, the internal tube is connected to fewer and thicker branches, which ramify with a wider angle.

The initial and final design performance curves in the objective space are shown

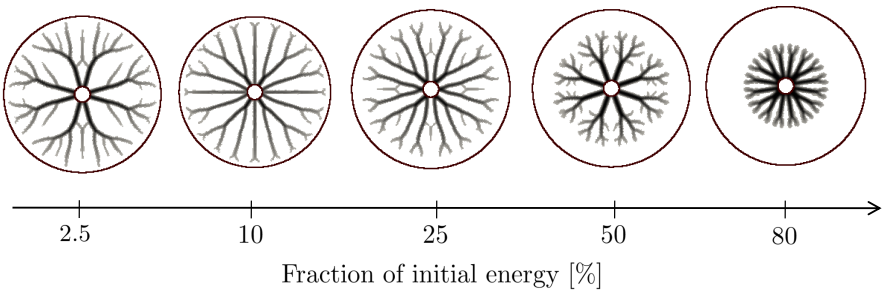

Figure 7. Final designs at selected Pareto points

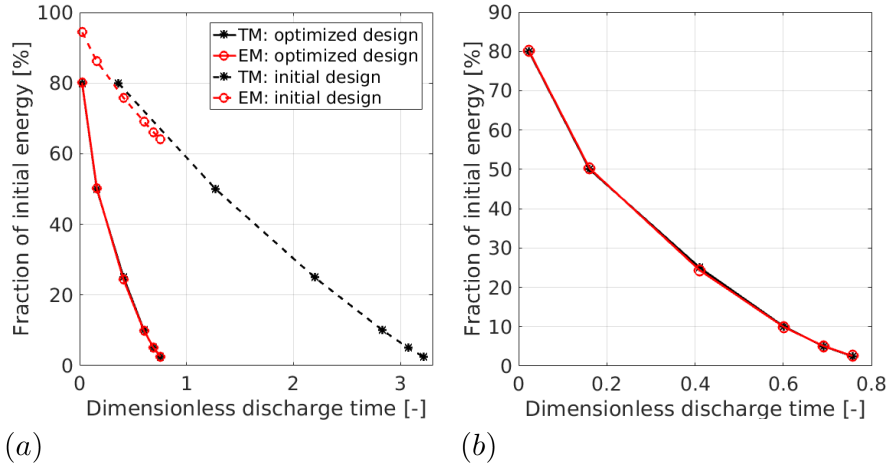

Figure 8. (a): Energy Minimization vs Time Minimization approach. (b): Converged Pareto curve

in Fig. 8.(a): the Time Minimization performance curve moves along the time axis (i.e. from right to left). On the other hand, the Energy Minimization performance curve moves along the energy axis (i.e. from top to bottom). Both the approaches converge to nearly the same Pareto front, with a maximum relative deviation of 2.6 %. The optimized performance curve is presented in Figure 8(b).

We now cross-check the performances of the Time Minimization designs with different residual energy targets Ψ. Each design optimized for a certain Ψ is expected to perform better than the other designs for that particular Ψ condition. If this is not the case, this test indicates convergence to poor local minima. For each optimized design, Figure 9(a) plots the discharge time increase compared to the optimized design for that particular Ψ. It can be seen that the optimized designs perform as expected. Moreover, we note that either a badly designed or

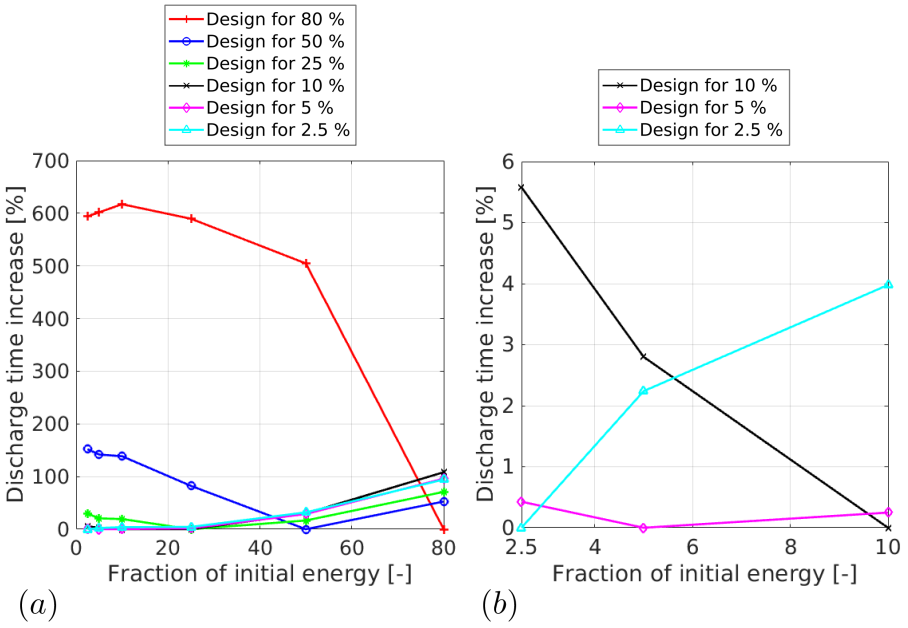

Figure 9. (a): Performance cross-check of optimized designs on other points on the Pareto front. The discharge time increase is calculated with respect to the design optimized for that particular Ψ. (b): zoom-in of the low-energy region

a badly utilized TES system can result in substantial performance reductions, highlighting the importance of an accurate prediction of the discharge dynamics during the design optimization process. For instance, if the design optimized for $\Psi = 80$ % is used to discharge the tank up to $\Psi = 10$ %, a 600 % time increase is needed with respect to the discharge of the design optimized for that situation. Taking a closer look at the low energy region (depicted in Fig. 9.(b)), which is meaningful from a TES application perspective, we observe a much more robust performance, i.e. the designs look slightly sensitive to changes in Ψ.

The results obtained in this numerical study demonstrate the equivalence of the first two optimization problem formulations proposed in Sec. 3, i.e. the Energy Minimization and the Time Minimization approach. Furthermore, we highlight the importance of an accurate modeling of the transient behavior for the design optimization of LHTES systems by outlining a well-defined Pareto curve in the space discharged energy/discharge time.

4.2. 3D designs

In this section, we extend the analysis performed in Sec. 4.1 to 3D design optimization using the Time Minimization approach. The 2D design domain in Figure 2 is linearly extruded along the z axis to obtain a quarter cylinder with height $Z = 3$. Adiabatic boundary conditions are applied at both ends.

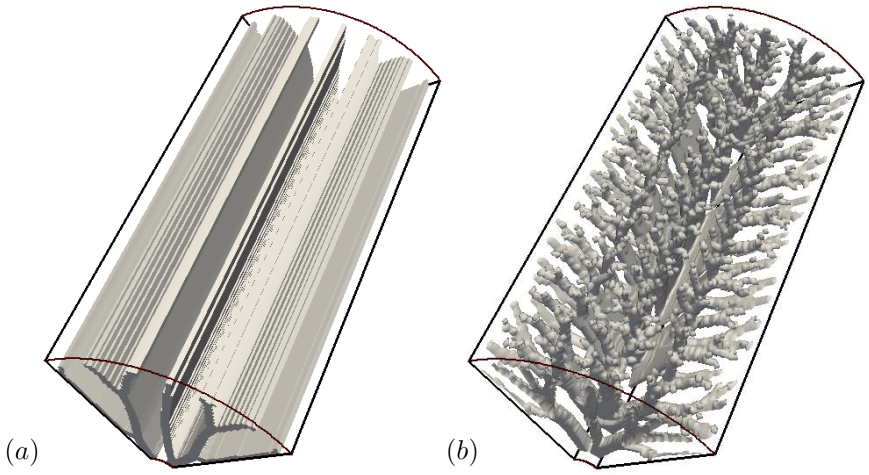

Figure 10. 2D extruded design (a) versus full 3D design visualization (b). Only a quarter of the cross-section is shown for clarity purposes. The design shown has been thresholded at $s = 0.1$

Figure 10 visualizes the main qualitative differences between the 2D and the 3D design for $\Psi = 5$ %. Please note that the design shown has again been thresholded at $s = 0.1$. Due to the good convergence to a binary design, the threshold value choice has a negligible effect. The 3D design is an interesting mixture of the different fins design discussed in the introductory section of this paper: longitudinal fins, radial fins, and pin fins. Similar to the radial fins designs, our optimized 3D design alternates high HCM density cross-sections to low density ones, leaving some PCM interstices along the z axis. Furthermore, the cross sections of our 3D design (Figure 11(b)) show a pattern similar to the 2D design. Finally, our HCM branch tips closely resemble the disordered geometries of the pin fins designs elongating freely in the three directions. The front and top views visible in Figure 11 display some additional features. As visible from the front view, the distribution of HCM concentrates more at the center than at the top and bottom boundary. This agrees with the intuition that less HCM should be placed on the boundary since less energy has to be extracted.

Finally, we revisit the energy versus time trade-off for 3D designs with 3 different values of energy fraction Ψ, i.e. 25 %, 10 % and 5 %. Figure 12(a) shows a comparison between the Pareto fronts for the 3D and the 2D case. Figure 12(b) presents a bar chart plotting both the absolute and percentage improvements achieved. We observe an average discharge time reduction of 20.3 %, with the minimum and maximum being 18.0 % and 22.6 % respectively.

This section highlights the need for full 3D optimization strategies for the

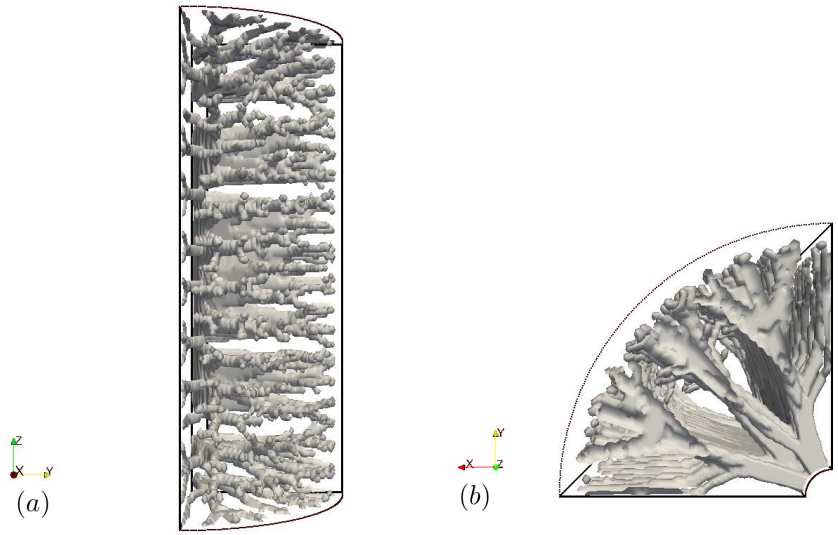

Figure 11. (a): Front view of 3D design. (b): Top view of 3D design

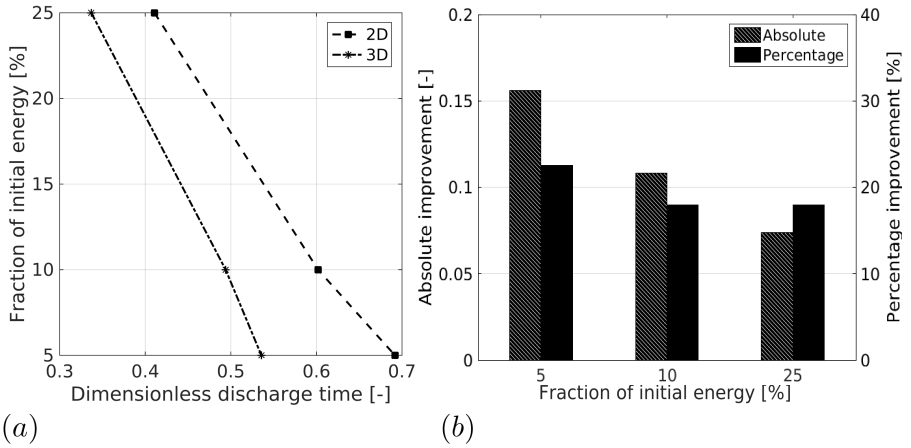

Figure 12. (a): 3D Pareto vs 2D Pareto obtained through the Time Minimization approach. (b): Absolute and percentage performance improvements of 3D designs in the three Pareto points considered

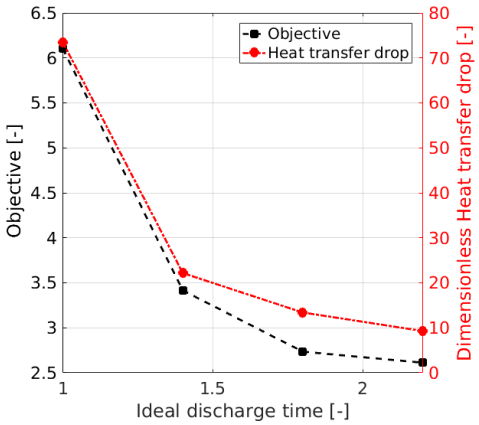

Figure 13. The time vs steadiness trade-off. The objective trend closely resembles the one of the heat transfer drop during the complete discharge

design of TES with phase change. The optimized design not only shows some unexpected features but it also outperforms the 2D one by roughly 20 % due to the increased design freedom.

4.3. Steadiness maximization

With this example we aim at showing how topology optimization can address more complicated and interesting objectives for the design of TES systems. Beside a low discharge time, which we discussed in the previous sections, one of the most desirable properties is to deliver a constant thermal power output during the whole discharge process. Hence, we adopt the optimization problem formulation presented in (27).

The optimized performance curves, obtained for a total discharge time of 1, 1.4, 1.8 and 2.2 are shown in Figure 13. In the range of values considered, we observe an interesting trade-off between allowable discharge time and steadiness of discharge. The objective drops from the initial value of 6.1 when $t^*_{f_{id}} = 1.0$ to the final value of 2.6 when when $t^*_{f_{id}} = 2.2$. On the right y-axis of Fig. 13 we plot the optimized heat transfer drop during the discharge history in the four cases considered. This figure of merit is intended to measure the steadiness in an alternative way; it is calculated as the difference between the initial and the final heat transfer rate.

The optimized distribution of highly conductive finning material for the four cases considered is shown in Figure 14. The "quick" design (i.e. $t^*_{f_{id}} = 1.0$) looks very close to the optimized designs of the previous section for the low Ψ region. As the discharge time increases, more and more highly conductive material is moved towards the external tank envelope through wide angle ramifications coupled to a higher number of secondary branches. Furthermore, it is possible to observe in the "slow" designs (e.g. $t^*_{f_{id}} = 1.8$ and $t^*_{f_{id}} = 2.2$)

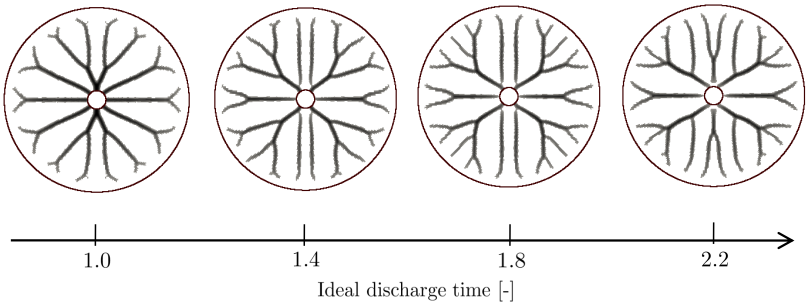

Figure 14. Steadiness optimized designs with different values of ideal discharge time $t^*_{f_{id}}$

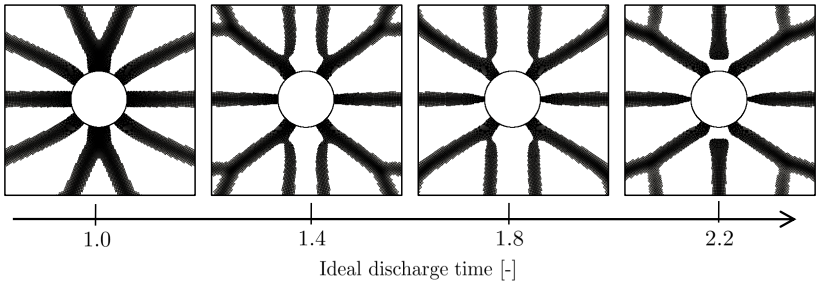

Figure 15. Detail of the fin base disconnect

that the fin base is not anymore in contact with the internal tube, leaving a small PCM gap. The authors believe that this is effective in limiting the initial heat transfer rate. The gap certainly complicates the fabrication of the fin. However, manufacturability is not considered in the optimization problem formulation and the practical realization of the device is beyond the scope of this paper. Topology optimization with manufacturability constraints has been investigated elsewhere, see e.g. [66]. For better visualization of the fin base disconnect, Figure 15 shows a zoomed-in view into the region close to the internal tube.

The discharge histories of the 4 optimized designs is pictured in Figure 16. Here, to enhance the readability and cross-comparison of data, we plot on the x-axis the discharge time normalized with respect to the ideal discharge time $t^*_{f_{id}}$. As the final time constraint is relaxed, the real energy history becomes closer and closer to the ideal linear one. However, even the optimized design for $t^*_{f_{id}} = 2.6$ does not perfectly match the desired discharge history. The reader may note the big performance improvement achievable if the allowable discharge

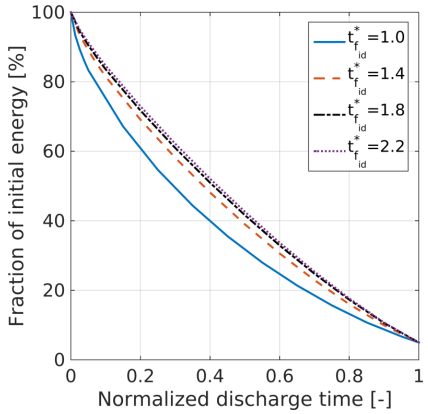

Figure 16. Normalized energy history during the discharge for the 4 optimized designs

Table 4. Comparison of the connected and disconnected design

	Connected design	Disconnected design
Discharge time	1.77	2.20
Objective	14.63	2.68

time is increased from 1.0 to 1.4.

To show that the fin disconnect increases the performance, we manually altered the design optimized for $t^*_{f_{id}} = 2.2$ (hereafter referred as disconnected design) and filled the PCM gap with HCM to obtain the connected design shown in Figure 17(a). The energy history for the two designs considered along with the ideal one are represented in Figure(b). The connected design yields a reduction of the total time needed for the discharge. However, the disconnected design approximates better the ideal discharge curve. The area enclosed between the ideal discharge curve and the one of the disconnected design, i.e. A_1, is smaller than the area enclosed between the ideal discharge curve and the one of the connected design, i.e. $A_1 + A_2$. This suggests that a superior objective value is obtained with the disconnected design. The objective value and the discharge time registered in the two cases are reported in Table 4.

Through this example we have shown that it is possible to tune the discharge history of the LHTES towards a constant thermal power output. It is also found that the steadiness measure increases if less stringent requirements are set on the discharge time.

5. Conclusions

We demonstrated the use of topology optimization for heat transfer enhancement in Latent Heat Thermal Energy Storage tanks. We optimized the layout of

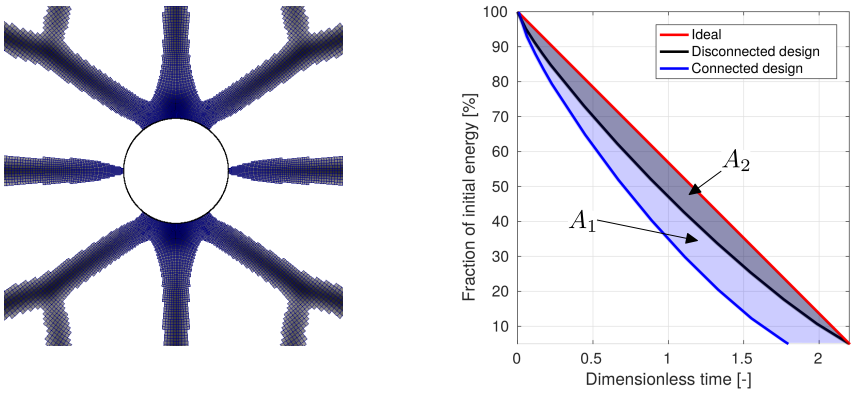

(a) (b)

Figure 17. (a): Connected version of the disconnected optimized design obtained for $t^*_{f_{id}} = 2.2$. (b): Comparison of the energy history during the discharge

a highly conductive material embedded in a phase change material to maximize the performance of the heat exchanger.

We first proposed two alternative problem formulations to fasten the discharge process: the Energy Minimization approach minimizes the residual energy in the tank at a fixed time while the Time Minimization approach minimizes the time required to discharge the tank down to a specified energy fraction. The 2D example showed that both approaches converge to the same Pareto front in the residual energy/discharge time space. The inherent trade-off between these two objectives manifests itself with very different designs and highly varying performances in different points of the non-dominated set. Furthermore, we found that the optimized designs in 3D presents features not visible in 2D which yield a discharge time reduction of roughly 20 % with respect to the 2D designs.

Finally, we focused on the HCM fins design that maximizes the steadiness of the thermal power output. We observed that relaxing the requirements on the maximum discharge time allows for better tuning of the tank discharge history: with a 40 % increase of the discharge time we obtain a 44 % improvement of our steadiness measure. A small PCM gap close to the internal tube is effective in lowering the initial heat transfer peak but complicates the manufacturing process.

The results demonstrate the convenience of topology optimization for the practical design of LHTES systems. The method yields design features and trends that could hardly be revealed with alternative design routes.

Acknowledgements

The third author acknowledges the support of the National Science Foundation under grant EFRI-SEED 1038305. The opinions and conclusions presented in this paper are those of the authors and do not necessarily reflect the views of the sponsoring organization.

References

[1] F. Colella, A. Sciacovelli, V. Verda, Numerical analysis of a medium scale latent energy storage unit for district heating systems, Energy 45 (1) (2012) 397–406.

[2] T.-C. Ling, C.-S. Poon, Use of phase change materials for thermal energy storage in concrete: an overview, Construction and Building Materials 46 (2013) 55–62.

[3] M. Pomianowski, P. Heiselberg, Y. Zhang, Review of thermal energy storage technologies based on pcm application in buildings, Energy and Buildings 67 (2013) 56–69.

[4] D. Zhou, C.-Y. Zhao, Y. Tian, Review on thermal energy storage with phase change materials (pcms) in building applications, Applied energy 92 (2012) 593–605.

[5] G. Serale, F. Goia, M. Perino, Numerical model and simulation of a solar thermal collector with slurry phase change material (pcm) as the heat transfer fluid, Solar Energy 134 (2016) 429–444.

[6] Z. Ling, Z. Zhang, G. Shi, X. Fang, L. Wang, X. Gao, Y. Fang, T. Xu, S. Wang, X. Liu, Review on thermal management systems using phase change materials for electronic components, li-ion batteries and photovoltaic modules, Renewable and Sustainable Energy Reviews 31 (2014) 427–438.

[7] R. Baby, C. Balaji, Experimental investigations on phase change material based finned heat sinks for electronic equipment cooling, International Journal of Heat and Mass Transfer 55 (5) (2012) 1642–1649.

[8] Y. Kozak, B. Abramzon, G. Ziskind, Experimental and numerical investigation of a hybrid pcm–air heat sink, Applied Thermal Engineering 59 (1) (2013) 142–152.

[9] B. Zalba, J. M. Marın, L. F. Cabeza, H. Mehling, Review on thermal energy storage with phase change: materials, heat transfer analysis and applications, Applied thermal engineering 23 (3) (2003) 251–283.

[10] A. Sharma, V. Tyagi, C. Chen, D. Buddhi, Review on thermal energy storage with phase change materials and applications, Renewable and Sustainable energy reviews 13 (2) (2009) 318–345.

[11] S. E. Kalnæs, B. P. Jelle, Phase change materials and products for building applications: a state-of-the-art review and future research opportunities, Energy and Buildings 94 (2015) 150–176.

[12] R. Parameshwaran, S. Kalaiselvam, S. Harikrishnan, A. Elayaperumal, Sustainable thermal energy storage technologies for buildings: a review, Renewable and Sustainable Energy Reviews 16 (5) (2012) 2394–2433.

[13] D. H. Choi, J. Lee, H. Hong, Y. T. Kang, Thermal conductivity and heat transfer performance enhancement of phase change materials (pcm) containing carbon additives for heat storage application, International Journal of Refrigeration 42 (2014) 112–120.

[14] P. Chandrasekaran, M. Cheralathan, V. Kumaresan, R. Velraj, Enhanced heat transfer characteristics of water based copper oxide nanofluid pcm (phase change material) in a spherical capsule during solidification for energy efficient cool thermal storage system, Energy 72 (2014) 636–642.

[15] L. Colla, L. Fedele, S. Mancin, L. Danza, O. Manca, Nano-pcms for enhanced energy storage and passive cooling applications, Applied Thermal Engineering 110 (2017) 584 – 589.

[16] R. Velraj, R. Seeniraj, B. Hafner, C. Faber, K. Schwarzer, Heat transfer enhancement in a latent heat storage system, Solar energy 65 (3) (1999) 171–180.

[17] X. Tong, J. A. Khan, M. RuhulAmin, Enhancement of heat transfer by inserting a metal matrix into a phase change material, Numerical Heat Transfer, Part A Applications 30 (2) (1996) 125–141.

[18] P. Griffiths, P. Eames, Performance of chilled ceiling panels using phase change material slurries as the heat transport medium, Applied Thermal Engineering 27 (10) (2007) 1756–1760.

[19] F. Agyenim, P. Eames, M. Smyth, Heat transfer enhancement in medium temperature thermal energy storage system using a multitube heat transfer array, Renewable Energy 35 (1) (2010) 198–207.

[20] R. Hendra, T. Mahlia, H. Masjuki, et al., Thermal and melting heat transfer characteristics in a latent heat storage system using mikro, Applied thermal engineering 25 (10) (2005) 1503–1515.

[21] M. Esapour, M. Hosseini, A. Ranjbar, Y. Pahamli, R. Bahrampoury, Phase change in multi-tube heat exchangers, Renewable Energy 85 (2016) 1017–1025.

[22] F. Agyenim, N. Hewitt, P. Eames, M. Smyth, A review of materials, heat transfer and phase change problem formulation for latent heat thermal energy storage systems (lhtess), Renewable and sustainable energy reviews 14 (2) (2010) 615–628.

[23] R. N. Smith, J. Koch, Numerical solution for freezing adjacent to a finned surface, in: Proceeding of the Seventh International Heat Transfer Conference, Vol. 74, Muchen, Germany, 1982.

[24] M. Lacroix, Study of the heat transfer behavior of a latent heat thermal energy storage unit with a finned tube, International Journal of Heat and Mass Transfer 36 (8) (1993) 2083–2092.

[25] K. Ismail, C. Alves, M. Modesto, Numerical and experimental study on the solidification of pcm around a vertical axially finned isothermal cylinder, Applied Thermal Engineering 21 (1) (2001) 53–77.

[26] K. Ermis, A. Erek, I. Dincer, Heat transfer analysis of phase change process in a finned-tube thermal energy storage system using artificial neural network, International Journal of Heat and Mass Transfer 50 (15) (2007) 3163–3175.

[27] N. Tay, F. Bruno, M. Belusko, Comparison of pinned and finned tubes in a phase change thermal energy storage system using cfd, Applied energy 104 (2013) 79–86.

[28] M. Hosseini, A. Ranjbar, M. Rahimi, R. Bahrampoury, Experimental and numerical evaluation of longitudinally finned latent heat thermal storage systems, Energy and Buildings 99 (2015) 263–272.

[29] A. Sciacovelli, F. Gagliardi, V. Verda, Maximization of performance of a pcm latent heat storage system with innovative fins, Applied Energy 137 (2015) 707–715.

[30] R. H. Myers, D. C. Montgomery, C. M. Anderson-Cook, Response surface methodology: process and product optimization using designed experiments, John Wiley & Sons, 2016.

[31] A. Sciacovelli, V. Verda, Second-law design of a latent heat thermal energy storage with branched fins, International Journal of Numerical Methods for Heat & Fluid Flow 26 (2) (2016) 489–503.

[32] M. P. Bendsøe, Optimal shape design as a material distribution problem, Structural optimization 1 (4) (1989) 193–202.

[33] M. Zhou, G. Rozvany, The coc algorithm, part ii: topological, geometrical and generalized shape optimization, Computer Methods in Applied Mechanics and Engineering 89 (1-3) (1991) 309–336.

[34] G. Allaire, F. Jouve, A.-M. Toader, Structural optimization using sensitivity analysis and a level-set method, Journal of Computational Physics 194 (1) (2004) 363–393.

[35] R. Behrou, M. Lawry, K. Maute, Level set topology optimization of structural problems with interface cohesion, International Journal for Numerical Methods in Engineering.

[36] Y. Xie, G. Steven, A simple evolutionary procedure for structural optimization, Computers & Structures 49 (5) (1993) 885–896.

[37] L. Xia, F. Fritzen, P. Breitkopf, Evolutionary topology optimization of elastoplastic structures, Structural and Multidisciplinary Optimization 55 (2) (2017) 569–581.

[38] O. Sigmund, K. Maute, Topology optimization approaches, Structural and Multidisciplinary Optimization 48 (6) (2013) 1031–1055.

[39] A. Gersborg-Hansen, O. Sigmund, R. B. Haber, Topology optimization of channel flow problems, Structural and Multidisciplinary Optimization 30 (3) (2005) 181–192.

[40] S. Kreissl, G. Pingen, K. Maute, Topology optimization for unsteady flow, International Journal for Numerical Methods in Engineering 87 (13) (2011) 1229–1253.

[41] S. Nørgaard, O. Sigmund, B. Lazarov, Topology optimization of unsteady flow problems using the lattice boltzmann method, Journal of Computational Physics 307 (2016) 291–307.

[42] E. Wadbro, M. Berggren, Topology optimization of an acoustic horn, Computer methods in applied mechanics and engineering 196 (1) (2006) 420–436.

[43] S. Halkjær, O. Sigmund, J. S. Jensen, Maximizing band gaps in plate structures, Structural and Multidisciplinary Optimization 32 (4) (2006) 263–275.

[44] K. Maute, M. Allen, Conceptual design of aeroelastic structures by topology optimization, Structural and Multidisciplinary Optimization 27 (1-2) (2004) 27–42.

[45] S. Zhou, W. Li, Q. Li, Level-set based topology optimization for electromagnetic dipole antenna design, Journal of Computational Physics 229 (19) (2010) 6915–6930.

[46] J. K. Guest, J. H. Prévost, Optimizing multifunctional materials: design of microstructures for maximized stiffness and fluid permeability, International Journal of Solids and Structures 43 (22) (2006) 7028–7047.

[47] M. P. Bendsoe, O. Sigmund, Topology optimization: theory, methods, and applications, Springer Science & Business Media, 2013.

[48] D. Makhija, K. Maute, Level set topology optimization of scalar transport problems, Structural and Multidisciplinary Optimization 51 (2) (2015) 267–285.

[49] G. H. Yoon, Topological design of heat dissipating structure with forced convective heat transfer, Journal of Mechanical Science and Technology 24 (6) (2010) 1225–1233.

[50] J. Alexandersen, N. Aage, C. S. Andreasen, O. Sigmund, Topology optimisation for natural convection problems, International Journal for Numerical Methods in Fluids 76 (10) (2014) 699–721.

[51] P. Coffin, K. Maute, A level-set method for steady-state and transient natural convection problems, Structural and Multidisciplinary Optimization 53 (5) (2016) 1047–1067.

[52] D. Castro, C. Kiyono, E. Silva, Design of radiative enclosures by using topology optimization, International Journal of Heat and Mass Transfer 88 (2015) 880–890.

[53] C. Zhuang, Z. Xiong, A global heat compliance measure based topology optimization for the transient heat conduction problem, Numerical Heat Transfer, Part B: Fundamentals 65 (5) (2014) 445–471.

[54] C. Zhuang, Z. Xiong, H. Ding, Topology optimization of the transient heat conduction problem on a triangular mesh, Numerical Heat Transfer, Part B: Fundamentals 64 (3) (2013) 239–262.

[55] V. Srinivas, G. Ananthasuresh, Analysis and topology optimization of heat sinks with a phase-change material on comsol multiphysics platform, in: COMSOL Users Conference, 2006, pp. 1–7.

[56] S. Jegadheeswaran, S. D. Pohekar, Performance enhancement in latent heat thermal storage system: a review, Renewable and Sustainable Energy Reviews 13 (9) (2009) 2225–2244.

[57] M. B. Giles, N. A. Pierce, An introduction to the adjoint approach to design, Flow, turbulence and combustion 65 (3-4) (2000) 393–415.

[58] O. Sigmund, J. Petersson, Numerical instabilities in topology optimization: a survey on procedures dealing with checkerboards, mesh-dependencies and local minima, Structural optimization 16 (1) (1998) 68–75.

[59] T. E. Bruns, D. A. Tortorelli, Topology optimization of non-linear elastic structures and compliant mechanisms, Computer Methods in Applied Mechanics and Engineering 190 (26) (2001) 3443–3459.

[60] F. Wang, B. S. Lazarov, O. Sigmund, On projection methods, convergence and robust formulations in topology optimization, Structural and Multidisciplinary Optimization 43 (6) (2011) 767–784.

[61] T. A. Davis, Algorithm 832: Umfpack v4. 3—an unsymmetric-pattern multifrontal method, ACM Transactions on Mathematical Software (TOMS) 30 (2) (2004) 196–199.

[62] Y. Saad, M. H. Schultz, Gmres: A generalized minimal residual algorithm for solving nonsymmetric linear systems, SIAM Journal on scientific and statistical computing 7 (3) (1986) 856–869.

[63] Y. Saad, Ilut: A dual threshold incomplete lu factorization, Numerical linear algebra with applications 1 (4) (1994) 387–402.

[64] K. Svanberg, A class of globally convergent optimization methods based on conservative convex separable approximations, SIAM Journal on Optimization 12 (2) 555–573.

[65] COMSOL, version 5.0, COMSOL Inc., Burlington, MA, USA, 2014.

[66] L. Harzheim, G. Graf, A review of optimization of cast parts using topology optimization, Structural and multidisciplinary optimization 31 (5) (2006) 388–399.